Topochemical Formation of Mesoporous MnO Crystals

Eric S. Toberer,* Jan P. Löfvander, and Ram Seshadri*

Materials Department and Materials Research Laboratory, University of California, Santa Barbara, California 93106-5121

Received October 11, 2005. Revised Manuscript Received November 22, 2005

Heating hausmanite $ZnMn_2O_4$ in a reducing atmosphere results in the formation of rock salt MnO with significant Zn substitution. Further heating at elevated temperatures under reducing conditions results in Zn being reduced and expelled in the vapor phase, leaving behind nearly pure rock salt MnO. Used judiciously, the volume loss associated with such vapor-phase leaching can be employed for the formation of mesoporous MnO crystals with connected 30−60 nm pores, through a process of topochemical conversion. In this contribution we examine in detail the driving forces which induce vapor-phase leaching as well as the interplay between crystallography and crystal morphology which permit these unusual materials to be formed.

Introduction

Porous materials find numerous uses in catalysis, separations, filtration, fuel cells, secondary batteries, and indeed any application which requires a static solid phase to contact a second fluid phase. Materials can be rendered porous in a number of different ways, depending on the size scales of the pores desired. In the size range between 10 and 1000 nm (meso- and macroporous materials), the usual techniques preparation involves the use sacrificial templates for pore formation. These templates include surfactant assemblies (in the preparation of MCM[1] materials), block copolymers (in the preparation of SBA[2] materials), or colloidal crystal templates (in the preparation of inverse opals[3]).

We have for some time been interested in preparing complex oxides with meso- and macroporous architectures using processes which obviate the need for preformed templates. The general strategy has been to form a dense *two-phase* monolith from which one of the two phases is selectively removed to leave behind a macroporous monolith of the other phase. Selective leaching of one phase from a two-phase composite has allowed us to form macroporous binary oxides and metals, as well as more complex materials in macroporous form, including functional perovskites such as $La_{0.7}Sr_{0.3}MnO_3$ and $PbTiO_3$.[4−6]

The technique of selectively leaching out one phase to create porosity has been traditionally used in the formation of porous Vycor glass through the dissolution of a borosilicate rich phase.[7] Selective leaching of an element from an alloy is a strategy dating back to the pre-Columbian era in which the luster of gold−silver alloys was improved by the dissolution of silver from the outer surface.[8] More recently, the formation of Raney nickel through selective leaching has become an industrially important method of forming high surface area porous metals.[9]

Along similar lines, Gorte, and co-workers have prepared porous solid oxide fuel cell cathodes by the selective removal of the Ni from a Y_2O_3-stabilized ZrO_2/Ni composite.[10] Suzuki et al. have used eutectic reactions to form two-phase monoliths for selective leaching.[11] Reactive sintering with release of CO_2 through decomposition of carbonate precursors is another strategy used by Suzuki et al. to prepare macroporous monoliths.[12]

We recently reported the formation of hierarchically porous rock salt MnO formed through two stages of successive leaching of chemical components starting from a two-phase monolith, as depicted schematically in Figure 1a.[13] Macropores first form through alkali leaching of the sacrificial wurtzite ZnO phase from a two-phase $ZnO/ZnMn_2O_4$ composite, as depicted in Figure 1b. The second stage of leaching involves the reduction and concurrent vapor-phase leaching of Zn from the ternary compound $ZnMn_2O_4$ (Figure 1c), leaving behind hierarchically porous rock salt MnO. To suppport our observations, we had performed sorption measurements and scanning electron microscopy (SEM).[13] In this contribution, we study the phase evolution during such vapor-phase leaching and characterize the resulting hierarchically porous structure using a combination of thermogravimetry, diffrac-

* To whom correspondence should be addressed: etoberer@engineering.ucsb.edu (E.S.T.), seshadri@mrl.ucsb.edu (R.S.).

(1) Beck, J. S.; Vartuli, J. C.; Roth, W. J.; Leonowicz, M. E.; Kresge, C. T.; Schmitt, K. D.; Chu, C. T. W.; Olson, D. H.; Sheppard, E. W.; McCullen, S. B.; Higgins, J. B.; Schlenker, J. L. *J. Am. Chem. Soc.* **1992**, *114*, 10834.
(2) Zhao, D.; Feng, J.; Huo, Q.; Melosh, N.; Fredrickson, G. H.; Chmelka, B. F.; Stucky, G. D. *Science* **1998**, *279*, 548.
(3) Holland, B. T.; Blanford, C. F.; Stein, A. *Science* **1998**, *281*, 538.
(4) Rajamathi, M.; Thimmaiah, S.; Morgan, P.; Seshadri, R. *J. Mater. Chem.* **2001**, *11*, 2489.
(5) Toberer, E. S.; Weaver, J. W.; Ramesha, K.; Seshadri, R. *Chem. Mater.* **2004**, *16*, 2194.
(6) Toberer, E. S.; Joshi, A.; Seshadri, R. *Chem. Mater.* **2005**, *17*, 2142.
(7) Levitz, P.; Ehret, G.; Sinha, S. K.; Drake, J. M. *J. Chem. Phys.* **1991**, *95*, 6151.
(8) Lechtman, H. *Sci. Am.* **1984**, *250*, 56.
(9) Raney, M. U.S. Patent 1,563,787, 1925.
(10) Kim, H.; da Rosa, C.; Boaro, M.; Vohs, J.; Gorte, R. *J. Am. Ceram. Soc.* **2002**, *85*, 1473.
(11) Suzuki, Y.; Yamada, T.; Sakakibara, S.; Ohji, T. *Ceram. Eng. Sci. Proc.* **2000**, *21*, 19.
(12) Suzuki, Y.; Kondo, N.; Ohji, T. *J. Am. Ceram. Soc.* **2003**, *86*, 1128.
(13) Toberer, E. S.; Seshadri, R. *Adv. Mater.* **2005**, 2244.

10.1021/cm052255n CCC: $33.50
Published on Web 01/21/2006

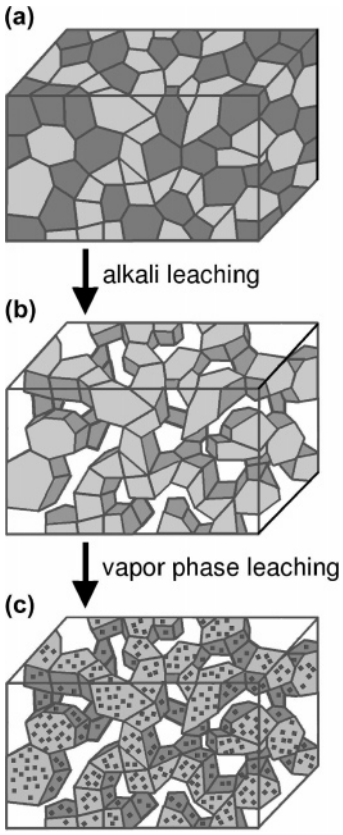

Figure 1. Scheme showing formation of hierarchically porous monoliths. Starting from a dense two-phase composite (a) of ZnO and $ZnMn_2O_4$, alkali leaching removes the ZnO phase, leaving macroporous $ZnMn_2O_4$ (b). Vapor-phase leaching of Zn in flowing hydrogen forms mesopores in the macropore walls of part b giving a hierarchically porous material (c).

tion, pore size measurements, and microscopy. Transmission electron microscopy (TEM) has allowed a detailed study of the crystallographic and morphological evolution during the leaching process. The studies demonstrate conclusively that the final materials are composed of mesoporous crystals of rock salt MnO with structures that could be described as biomimetic in their resemblance to the single-crystalline skeletal plates of sea urchins.[14−16]

Experimental Section

Zinc acetate [$Zn(CH_3CO_2)_2 \cdot 2H_2O$ (quantity 21.95 g)] and Mn acetate [$Mn(CH_3CO_2)_2 \cdot 4H_2O$ (quantity 9.80 g)] were dissolved in 2 L of water and quantitatively precipitated with 500 cm^3 of 0.5 M oxalic acid. The resulting oxalate [$Zn_{0.71}Mn_{0.29}(C_2O_4) \cdot 2H_2O$] formed immediately and was repeatedly washed. After drying, the oxalate precipitate was calcined as a powder at 873 K for 1 h in air to obtain oxides. The resulting powder was ground by hand with an agate mortar and pestle and then pressed into cylindrical pellets (13 mm in diameter and approximately 1−2 mm in height). Sintering of the oxides was achieved by calcining the pellets in air at 1473 K for 12 h. This sintering resulted in a two-phase composite from which the wurtzite ZnO phase could be removed by placing the pellets in 250 cm^3 of 4 M NaOH at 337 K for 3 days, with the solution being replaced twice. The macroporous pellets of $ZnMn_2O_4$ so obtained were washed in deionized water for a day with periodic replacement of the water. Drying was achieved in an air oven at 353 K.

The same coprecipitation method was also used to form the oxalate, [$Zn_{0.33}Mn_{0.67}(C_2O_4) \cdot 2H_2O$], the decomposition and sintering of which resulted in the pure, dense compound $ZnMn_2O_4$.

Vapor-phase leaching of both the porous and the dense $ZnMn_2O_4$ pellets was carried out in a tube furnace under flowing 5% H_2/N_2. The furnace was ramped to the reaction temperature at 3 K/min and held for 4−12 h. Hydrochloric acid was used to clean the accumulated Zn from the insides of the reaction tube between heatings.

Powder X-ray diffraction (XRD) was recorded for all samples on a Scintag X2 diffractometer in the $\theta-2\theta$ geometry and using Cu Kα radiation, with a step size of 0.015° 2θ and step time of 4 s per step. The diffractometer was operated at 45 kV and 35 mA. Rietveld refinements of the diffraction data were performed with the XND code.[17]

SEM was performed using a FEI XL40 Sirion microscope. Samples for microscopy were prepared from the interior fracture surfaces of broken pellets. The samples were mounted on double-sided carbon tape and were gold-coated before imaging.

Thermogravimetry measurements of $ZnMn_2O_4$ powder were obtained on a Mettler TGA/STGA 851E with a temperature ramp of 2 K/min under flowing 5% H_2/N_2. Thermodiffraction was initially performed in a reducing atmosphere on a Bruker D8 Advance instrument using a platinum heating stage, but these measurements could not be used as the evolved Zn vapor reacted with the stage. As an alternative, we have followed here a series of reductions in a tube furnace, by ex situ XRD. A ramp rate of 2 K/min was used to reach a set temperature, which was held for 30 min, and to rapidly cool.

Nitrogen sorption measurements were acquired on a Micrometrics TriStar 3000 instrument at 77 K.

Two samples were investigated with TEM: a reduced sample which was held at 725 K in a hydrogen atmosphere for 2 h and a reduced and leached sample which was held at 925 K for 12 h. Samples for TEM were prepared as thin sections by repeatedly immersing monoliths in M-Bond 610 epoxy under vacuum and then polishing. A FEI 235 focused ion beam (FIB) was used to then prepare 14 μm by 4 μm by 100 nm lamellae. The lamellae were placed on carbon TEM grids and studied in a FEI-T20 microscope operating at 200 keV.

Results and Discussion

Phase and Morphology. As described in our previous work, phase evolution during conversion has been studied by powder diffraction and SEM imaging of pellet cross sections.[13] The starting composite of ZnO and $ZnMn_2O_4$ showed by XRD Rietveld analysis a 9:1 mole ratio for the wurtzite/hausmanite phases (70:30 volume percent). SEM shows a dense material composed of 1 μm grains (Figure 2a). Compositions of the two different phases could be mapped, and the two phases thereby distinguished, using energy-dispersive X-ray analysis following the signal from Mn. Alkali leaching removes the ZnO phase, leaving behind a macroporous monolith of $ZnMn_2O_4$ (Figure 2b). Complete removal of the wurtzite ZnO phase is confirmed by XRD. The removal can be anticipated as the ZnO phase is present

(14) Donnay, G.; Pawson, D. L. *Science* **1969**, *166*, 1147.
(15) Meldrum, F. C.; Seshadri, R. *J. Chem. Soc., Chem. Commun.* **2000**, 29.
(16) Ha, Y.-H.; Vaia, R. A.; Lynn, W. F.; Costantino, J. P.; Shin, J.; Smith, A. B.; Matsudaira, P. T.; Thomas, E. L. *Adv. Mater.* **2004**, *16*, 1091.
(17) Bérar, J.-F.; Garnier, P. *NIST Spec. Publ.* **1992**, *846*, 212 (freely available from the CCP14 website at http://www.ccp14.ac.uk).

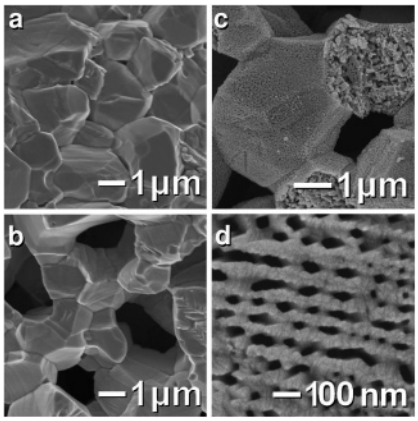

Figure 2. (a) SEM images of the dense composite pellet of ZnO and $ZnMn_2O_4$ and (b) of macroporous $ZnMn_2O_4$ following alkali leaching. (c) Fracture surface of the hierarchically porous monolith showing the mesopores that have developed in the walls of the material. (d) Mesopores at higher magnification.

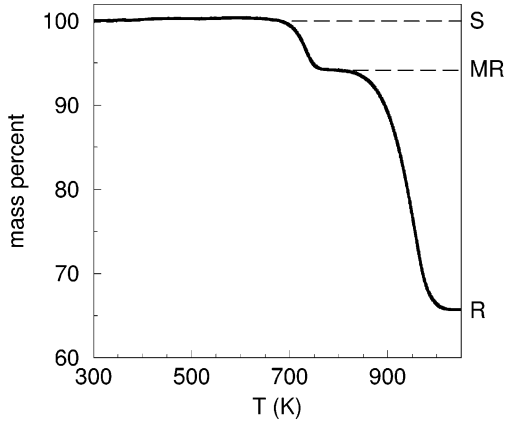

Figure 3. Thermogravimetric data obtained in a 5% H_2/N_2 atmosphere showing oxygen loss at 670 K due to conversion from $ZnMn_2O_4$ spinel (S) to $Zn_{0.33}Mn_{0.67}O$ metastable rock salt (MR). Further heating results in zinc/oxygen loss at 850 K leaving behind the MnO rock salt (R).

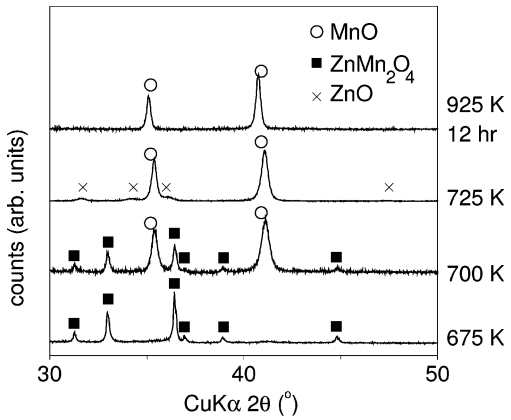

Figure 4. Powder XRD traces for $ZnMn_2O_4$ heated between 675 and 925 K in a reducing atmosphere (5% H_2/N_2). The transformation to Zn substituted MnO begins at by 675 K and is nearly complete by 725 K. Some partitioning of the Zn out of the rock salt is evident as wurtzite. The top trace shows the resulting MnO peaks after heating at 925 K for 12 h.

at a level that is well above the percolation threshold (17%) for a binary mixture of equal-sized spheres.[18] This implies that the porous network that is left behind is connected.

Subsequent reduction of this macroporous monolith under flowing 5% H_2/N_2 results in the conversion of the spinel to rock salt $Zn_{0.33}Mn_{0.67}O$. The decrease in material volume as a consequence of the transformation results in mesopores forming in the walls of the macroporous material. Vapor-phase leaching of Zn and its oxygen counterion further enlarge these mesopores. Figure 2c shows the fractured inner surface of a reduced and leached pellet. Mesopores are shown at a higher magnification in Figure 2d. The mesopores are self-affine and have right-angled edges, with typical edge lengths of 50 nm. This morphology suggests that the $ZnMn_2O_4$ to MnO conversion takes place in a manner that is crystallographically controlled.

We note here that exposing other spinels, such as $ZnFe_2O_4$, and also compounds containing Co or Ni result in direct conversion of the transition metal ion to the zerovalent metal.[6] Reduction of $ZnFe_2O_4$ in flowing 5% H_2/N_2, for example, gives macroporous Fe metal, the rapid sintering of the metal ensuring that any mesopores that are formed quickly close up. Phase formation in the title system emphasizes the importance of selecting for the process of vapor-phase leaching transition elements that are not easily reduced to the metal.

Thermal Evolution. To minimize coarsening of the pore network, it is desirable to carry out vapor-phase leaching at the lowest possible temperature. The onset of reduction and of Zn volatilization was determined by thermogravimetric measurements, displayed in Figure 3, of a $ZnMn_2O_4$ powder under flowing 5% H_2/N_2. The first drop in mass at 670 K corresponds to the loss of oxygen due to the reduction of Mn^{3+} to Mn^{2+} (weight percent loss: experimental, 6.3%; calculated, 6.6%). Beginning at 850 K, a larger mass loss is observed due to the reduction and evaporation of Zn and its corresponding oxide counterion from the MnO lattice (weight loss: experimental, 28.3%; calculated, 36.4%). Thus, 80% of the Zn ions have been removed from the rock salt lattice, leaving behind $Zn_{0.1}Mn_{0.9}$. The amount of Zn that remains dissolved in the MnO is approximately the thermodynamic solubility limit at these temperatures.

To monitor the phase evolution during the reduction and leaching process, a series of short reductions were performed, and the products were monitored by XRD. Beginning with macroporous $ZnMn_2O_4$, Figure 4 shows that after heating in flowing 5% H_2/N_2 at 675 K for 30 min, spinel is still the dominant phase present. In agreement with the thermogravimetric analysis (TGA) data, the reduction of Mn^{3+} to Mn^{2+} with the corresponding spinel to rock salt transformation begins near 675 K, and by 725 K, all of the spinel has been reduced to the Zn substituted MnO rock salt phase. Excess Zn in the metastable $Zn_{0.33}Mn_{0.66}O$ begins to partition out as wurtzite by 725 K. Quantitative phase analysis from Rietveld scale factors indicates that the wurtzite phase is never more than 8 mol % percent. High Zn levels in the rock salt phase are reflected in the MnO unit cell volume of 84.94 Å, compared to 87.9 Å for pure MnO.

Unusually, we find that the willingness of Zn to be reduced to the metal and then volatilized is strongly a function of the zinc ions being a part, initially, of a ternary $ZnMn_2O_4$ phase. This is clearly demonstrated when a dense composite of ZnO and $ZnMn_2O_4$ is subject to reduction and vapor-phase

(18) Heaney, M. B. *Phys. Rev. B* **1995**, *52*, 12477.

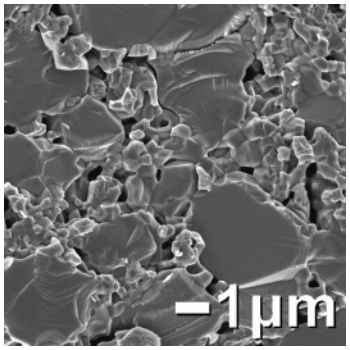

Figure 5. SEM image showing a $ZnO/Zn_{0.1}Mn_{0.9}O$ composite resulting from vapor-phase leaching of a dense $ZnO/ZnMn_2O_4$ composite at 925 K for 12 h. Pore formation and pitting are found to take place preferentially in the crystals which were initially $ZnMn_2O_4$, while the larger ZnO crystals are almost unaffected.

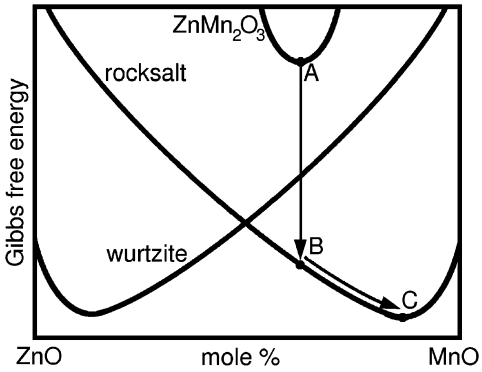

Figure 6. Scheme showing the large energy gain available in the conversion of the oxygen-deficient spinel (A) to rock salt (B). The free energy of the system may be further reduced by expulsion of Zn from the rock salt lattice (B to C).

leaching. The SEM image in Figure 5 shows such a two-phase composite after hydrogen reduction. The grains of $Zn_{0.1}Mn_{0.9}O$ formed from what was initially $ZnMn_2O_4$ display pitting and porosity characteristic of reduction and leaching. The larger wurtzite ZnO grains on the other hand are virtually unaffected by the treatment. When the leaching process is carried on for a longer time, the ZnO phase is eventually removed. In preliminary experiments, we have found that Zn_2TiO_4 and $ZnAl_2O_4$ behave quite differently from $ZnMn_2O_4$ in their reduction and leaching behavior, suggesting that the redox properties of the different cations play a significant role.

The preferential leaching of Zn from the metastable rock salt may be described in a qualitative free-energy diagram for ZnO and MnO. From TGA measurements, the Mn has become divalent by 670 K. The oxygen deficient hausmanite, $ZnMn_2O_3$, is not stable, and from the high temperature powder XRD pattern, we observe that the oxygen loss occurs concurrently with the transformation to the rock salt structure. The free-energy scheme in Figure 6 depicts this transformation from the hausmanite $ZnMn_2O_3$ (A) to rock salt $Zn_{0.33}Mn_{0.67}O$ (B) as corresponding to a large stabilization. Once the metastable rock salt has been formed, there are two options to further decrease the free-energy: partitioning of wurtzite ZnO from the rock salt lattice or a decrease in the concentration of Zn in the rock salt, through reduction and vapor-phase leaching. From the high-temperature XRD studies we find that both processes do occur, although the direct leaching of Zn from the rock salt lattice appears to dominate (B to C). We find that wurtzite is not stable above 875 K in flowing 5% H_2/N_2, and any wurtzite that is observed is formed during the ramp to the leaching temperature.

Table 1. Nitrogen Sorption Measurements of Macroporous $ZnMn_2O_4$ and $Zn_{0.33}Mn_{0.67}O$, Formed through Reduction at 725 K, and $Zn_{0.1}Mn_{0.9}O$ after Reduction/Leaching at 925 K[a]

	BET and BJH pore measurements				
	SA (m^2/g)	pore *d* (nm)	cum. vol ($cm^3\ g^{-1}$)	porosity (10−200 nm) measured	porosity (10−200 nm) expected
$ZnMn_2O_4$	1.3		0.004	2%	0%
$Zn_{0.33}Mn_{0.67}O$	9.8	30	0.039	17.5%	13.0%
$Zn_{0.1}Mn_{0.9}O$	13.5	50	0.10	35.0%	35.5%

[a] Surface area (SA), average pore diameter (*d*), and cumulative pore volume in the 10−200 nm range are presented. The measured porosity is expressed in volume percent and compared with what is expected given changes in structure and composition.

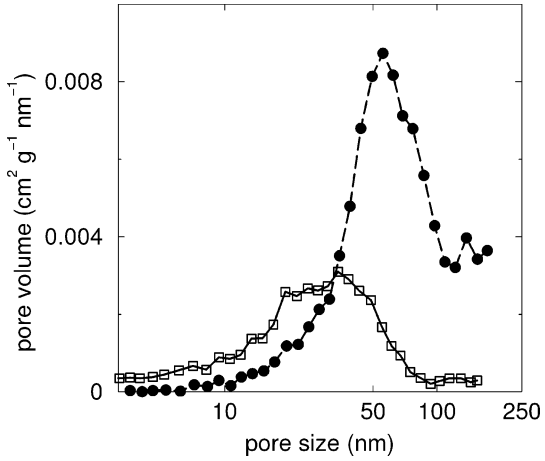

Figure 7. BJH pore size distributions for the metastable rock salt $Zn_{0.33}Mn_{0.67}O$ formed from heating at 725 K for 2 h (□) and after reduction and vapor-phase leaching at 925 K for 12 h to give $Zn_{0.1}Mn_{0.9}O$ (●).

Characterization of Porosity. Nitrogen sorption measurements were obtained at several stages during the leaching process: following alkali leaching of the two-phase $ZnO/ZnMn_2O_4$ composite, after reduction from the spinel to rock salt, and after vapor-phase leaching of the Zn from the rock salt. As shown in Table 1, macroporous $ZnMn_2O_4$ showed a low surface area, as expected for a purely macroporous material with effectively no porosity in the 10−200 nm regime. Interestingly, after reducing the macroporous $ZnMn_2O_4$ at 724 K in hydrogen for 2 h, the surface area increases by an order of magnitude. In addition, the Barrett−Joyner−Halenda (BJH) pore size distribution shows a peak at 30 nm and a cumulative pore volume in the 10−200 nm regime that corresponds to the expected volume change that accompanies the spinel to rock salt conversion (Figure 7). Leaching Zn and O from the sample at 925 K enlarges the average pore diameter to 50 nm and further increases the cumulative pore volume. The cumulative pore volume in the 10−200 nm range matches the volume change expected for the spinel to leached rock salt ($Zn_{0.1}Mn_{0.9}O$) conversion. These results suggest that all volume loss associated with chemical changes and the loss of ions are expressed through the formation of mesopores rather than as a compaction of material.

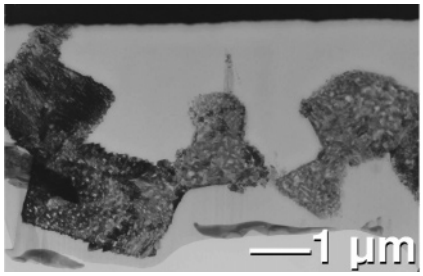

Figure 8. TEM micrograph of the FIB lamella at low magnification showing interconnected grains, as well as mesopores which penetrate into the grains. The black strip at the top is a layer of platinum deposited during the FIB process. Pores are seen from density contrast through the lamella.

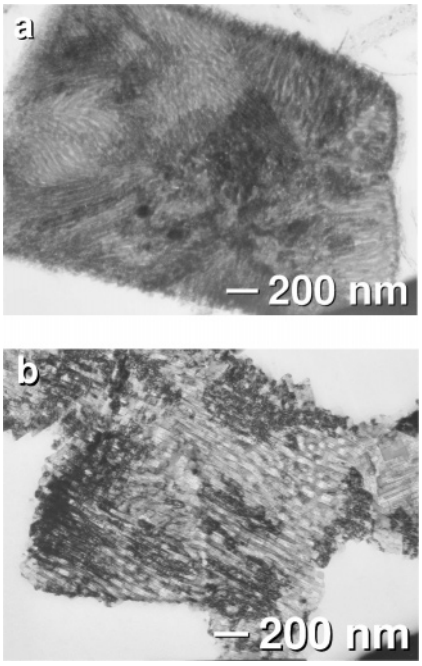

Figure 9. (a) Several collections of self-affine pores visible across a single grain of the $Zn_{0.33}Mn_{0.67}O$ sample formed at 725 K in a reducing atmosphere. (b) Cross section through a grain of $Zn_{0.1}Mn_{0.9}O$ formed from reduction and vapor-phase leaching at 925 K for 12 h.

Crystallography and Pore Structure. The self-affine arrangement of pores observed with SEM was investigated by TEM to determine relationships between the pore orientation and the crystallographic directions of each grain. Two hierarchically porous samples were analyzed: a reduced sample formed at 725 K in hydrogen and a sample which was reduced and leached in hydrogen at 925 K. The sample reduced at lower temperature comprised Zn-rich rock salt MnO, with a composition near $Zn_{0.33}Mn_{0.67}O$. The higher temperature treatment of the 925 K sample results both in reduction and in leaching of Zn, and the composition is close to $Zn_{0.1}Mn_{0.9}O$.

Electron transparent specimens were prepared using a FIB. Connected grains, 1 μm in diameter, are visible at low magnification in the TEM micrograph (Figure 8). Each grain has contrast variation across it from the presence of mesopores, while the gray region around the grains is the epoxy. Figure 9a displays several regions of aligned pores in the sample reduced at 725 K. Figure 9b shows the sample of $Zn_{0.1}Mn_{0.9}O$, reduced and leached at 925 K; it is clear in this latter sample that the mesopores have increased in size to about 50 nm, have right-angled edges, and are self-affine.

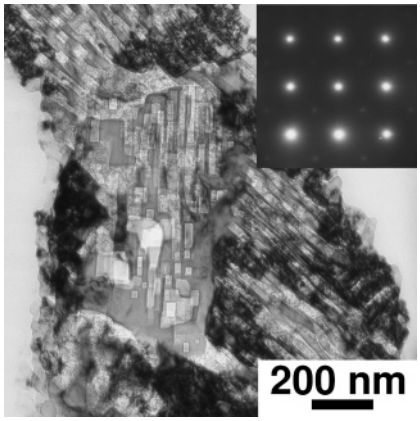

Figure 10. Transmission electron micrograph of regions of aligned pores. The pore size is approximately 50 nm, and the pore walls have right-angled edges and are composed of {100} crystal faces. The inset shows the diffraction pattern along the [001] zone axis micrograph obtained from the region on the left which has pores aligned vertically with the page.

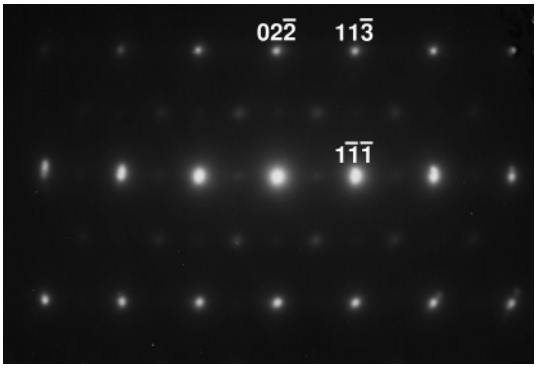

Figure 11. [211] zone axis electron diffraction pattern. $\{02\bar{2}\}$ and $\{1\bar{1}\bar{1}\}$ reflections are indicated, and superlattice reflections of $\{01\bar{1}\}$ and $\{^1/_2, \bar{1}/_2, \bar{1}/_2\}$ are present. $\{01\bar{1}\}$ superlattice reflections were clearly visible on the original negative but very faint in reproductions.

Electron diffraction on the sample reduced/leached at 925 K reveals that it is composed of crystalline grains ranging in extent between 400 and 800 nm. This was determined by tilting to a zone axis on a small area of the sample. The diffraction conditions then make it easy to establish the size of the crystalline region in the zone axis. The [100] zone axis diffraction (inset of Figure 10) is perfectly aligned with lines corresponding to pores in the central part of the real-space image (Figure 10). From this, we can conclude that the pore *morphology* is correlated with the pore wall *crystallography*, and the pore walls are made up of {100} crystal faces, which are the lowest energy faces of the rock salt lattice. These porous crystals are reminiscent of the porous crystals found in sea urchin spines and in their synthetic replicas.[14−16]

Electron diffraction patterns for the sample reduced at 725 K show the patterns expected for rock salt MnO. A pattern obtained along the [211] zone is shown in Figure 11, with $\{02\bar{2}\}$ and $\{1\bar{1}\bar{1}\}$ reflections visible. Surprisingly, there are also forbidden reflections present such as $\{01\bar{1}\}$ as well as superlattice $\{^1/_2, \bar{1}/_2, \bar{1}/_2\}$.

Similar extra reflections are also obtained for the sample reduced/leached at 925 K. This is seen in Figure 12, for the [110] zone axis, with the diffraction spots indexed as {200} and {220} marked. Close inspection reveals weaker reflections at half the distance (from the direct beam) of the

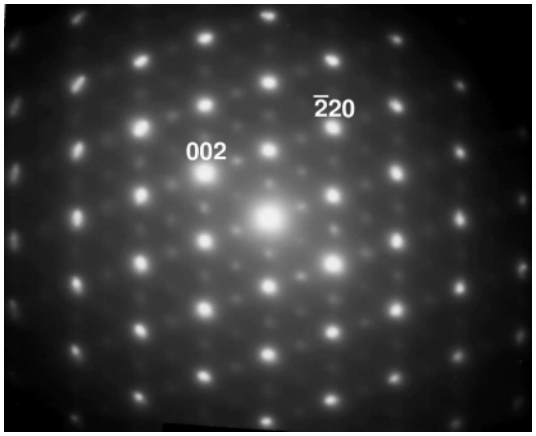

Figure 12. [110] zone axis diffraction pattern. {002} and {$\bar{2}$20} reflections are visible, as well as {100} and {$\bar{1}$10} superlattice peaks.

primary reflections corresponding to {100} and {110}, both of which are forbidden for face-centered cubic (fcc) rock salt. In addition, weak {$^1/_2$,$^1/_2$,$^1/_2$} superlattice reflections are also observed. We attribute these forbidden reflections, as well as the superlattice, as arising as a result of ordered Zn substitution (10% for this sample) for the Mn in the rock salt structure. Such ordering reflects the topochemical conversion of spinel to rock salt. We are unable at this stage to pinpoint the nature of this superstructure. We do note the existence of the compound $MnMg_6O_8$ which has an ordered rock salt structure in the fcc $Fm\bar{3}m$ space group with a cell parameter near 8.3 Å;[19] the extra reflections that we observe can be accounted for using a cell parameter of ≈8.8 Å, in the $Fm\bar{3}m$ space group. We note that neither is the ordering sufficiently coherent nor the atomic number contrast between Zn and Mn sufficiently large that the superlattice can observed in the XRD patterns.

Acknowledgment. We thank Michael Hayward and Susanne Stemmer for useful discussions and Abhijeet Joshi for contributing to the initial stages of this work. E.S.T. is supported by an IGERT fellowship from the NSF (Award No. DGE-9987618). This work was supported by the National Science Foundation through the Chemical Bonding Center (CHE-0434567) and made use of MRL facilities (DMR-0520415).

CM052255N

(19) Kasper, J. S.; Prener, J. S. *Acta Crystallogr.* **1954**, *7*, 246.